Journal of Materials Chemistry C

ROYAL SOCIETY OF CHEMISTRY

PAPER

View Article Online
View Journal

Cite this: DOI: 10.1039/d5tc04307g

Reversible hydration-induced ionic conductivity switching accompanied by large desorption enthalpy in sodium salts of 1,2,3-triazole-fused *p*-benzoquinone

Shiori Harada,[a] Shun Dekura, *[ab] Genki Saito,[a] Tetsu Sato[ab] and Tomoyuki Akutagawa *[ab]

Stimuli-responsive molecular solids that exhibit multifunctionality are highly sought after for advanced sensing and thermal energy storage applications. However, introducing guest molecules such as water into dense π-conjugated crystal lattices reversibly, while simultaneously achieving significant property modulation, remains a challenge. Herein, we demonstrate that the stepwise substitution of protons with sodium ions in 1,2,3-triazole-fused *p*-benzoquinone (**H_2BTBQ**) enables the control of flexibility and hydrophilicity of the crystal lattice, leading to reversible hydration-induced functionality switching. While the neutral form **H_2BTBQ** is anhydrous and insulating, the sodium salts **NaHBTBQ** and **Na_2BTBQ** form stable hydrates. Notably, **Na_2BTBQ** exhibits a reversible two-step water sorption behavior involving four water molecules per formula unit. Thermal analyses revealed that the dehydration of **Na_2BTBQ**·4H_2O is accompanied by a large endothermic enthalpy change (50.45 and 57.05 kJ (mol-H_2O)$^{-1}$), which significantly exceeds the heat of vaporization of bulk water, indicating its potential as a solid-state cooling material. Furthermore, alternating current (AC) impedance spectroscopy demonstrated that water adsorption triggers a drastic switching of ionic conductivity in **Na_2BTBQ**, originating from hydrated sodium ion migration. This work provides a crystal engineering strategy to realize functional materials combining large latent heat storage and dielectric switching *via* reversible hydration in dense organic salt crystals.

Received 8th December 2025,
Accepted 23rd February 2026

DOI: 10.1039/d5tc04307g

rsc.li/materials-c

Introduction

Crystalline organic solids composed of π-conjugated molecules have attracted significant attention in recent years due to their design flexibility, high responsiveness to external stimuli, and suitability for fundamental studies on structure–property relationships.[1–4] Based on diverse molecular designs and understanding of property-emergence mechanisms, various functionalities such as electronic conductivity,[5–7] (anti-)ferromagnetism,[8,9] ferroelectricity,[10–13] and anisotropic optical properties[14,15] have been developed in π-conjugated molecular solids, which are expected to find applications in transparent electrodes, spintronic devices, ferroelectric memories, and liquid crystal display materials. Recently, unconventional functionalities such as ambipolar field-effect transistors (FETs),[2,16,17] altermagnetism,[18] and anhydrous proton conductivity[19–25] have also been reported, paving the way for next-generation devices. Such functionalities of molecular assemblies heavily depend on the arrangement of the constituent molecules; fundamental studies on structure–property relationships are highly important.

On the other hand, environment-responsive organic materials are widely studied because they can visualize toxic/explosive gases or humidity changes by altering their optical or electrical properties in response to environmental changes.[26–29] Among them, materials that respond to water molecules—ubiquitous in the atmosphere—are attracting attention not only as humidity sensors that exhibit functional switching upon humidity changes but also as cooling materials utilizing adsorption heat.[30,31] In particular, organic solids without permanent porosity adsorb guest water molecules into their dense molecular assemblies inducing drastic molecular rearrangements. This process is expected to exhibit large latent heat due to the combination of structural changes and host–guest interactions. In particular, organic salt hydrates have been proposed as better candidates for adsorption thermal storage materials than conventional inorganic salt hydrates because of their reversible water sorption properties without showing deliquescence.[32,33] However, such non-porous organic materials typically show a high barrier to incorporating water molecules into their dense

[a] *Graduate School of Engineering, Tohoku University, Sendai 980-8579, Japan*
[b] *Institute of Multidisciplinary Research for Advanced Materials (IMRAM), Tohoku University, 2-1-1 Katahira, Aoba-ku, Sendai 980-8577, Japan. E-mail: s.dekura@tohoku.ac.jp*

molecular assemblies, and rational materials design guidelines for reversible water sorption have not been established. Furthermore, materials that simultaneously demonstrate heat storage and functionality switching induced by reversible water sorption have not been well explored.

To realize functionality switching *via* reversible water sorption, employing functional π-conjugated molecules as host materials is a promising approach.[28,30,34] However, since π-conjugated molecules are generally planar and rigid, they tend to form strong stacking columns through robust π–π interactions, which makes it difficult to reversibly introduce guest molecules under moderate conditions. We previously reported reversible water sorption and proton conductivity switching accompanied by an amorphous–crystal transition in non-planar saddle-shaped π-molecules.[27] In another case, we reported that alkali metal salts of planar naphthalenediimide (NDI) derivatives can reversibly incorporate water molecules despite having stable and dense assembly structures, enabling dielectric response switching while maintaining electronic conductivity.[28,30,34] The latter example particularly suggests that even for rigid planar π-conjugated host molecules, salt formation with alkali metals can facilitate reversible water sorption through the flexible coordination geometry and isotropic electrostatic interactions of alkali metal cations.

In this study, we focused on bis(1,2,3-triazole)-*p*-benzoquinone (=**H_2BTBQ**) and its sodium salts (**NaHBTBQ**, **Na_2BTBQ**; Scheme 1), which possess a planar π-conjugated skeleton and multiple proton donor/acceptor sites. Previous studies have reported the crystal structures and redox properties of **Na_nH_{2-n}BTBQ** (n = 0, 1, 2) in solution as well as thermogravimetry in solid state;[35,36] however, their solid-state functionalities including water sorption behaviors remained unexplored. Notably, since **Na_nH_{2-n}BTBQ** allows for sequential H^+/Na^+ exchange, the flexibility of the crystal lattice and host–guest interactions with water can be modulated stepwise, offering the potential to control reversible water sorption, heat storage, and functionality switching behaviors. In this paper, we investigated the hydration behavior, dehydration enthalpies *via* thermal measurements, water vapor sorption isotherms, and dielectric property changes accompanying reversible water sorption associated with the sequential H^+/Na^+ exchange in **Na_nH_{2-n}BTBQ** (n = 0, 1, 2). The sequential H^+/Na^+ exchange in **Na_nH_{2-n}BTBQ** induces reversible water sorption capability in the crystal lattice. Specifically, **Na_2BTBQ** exhibited multi-step water sorption behavior accompanied by structural changes. Surprisingly, the endothermic heat associated with this two-step dehydration significantly exceeded the heat of vaporization of water, suggesting its potential performance comparable to existing inorganic salt hydrates as solid-state thermal storage materials. Furthermore, **Na_2BTBQ** exhibited the emergence of dielectric response and ionic conductivity upon water adsorption, successfully realizing a multi-functional material combining heat storage capability with electrical property switching.

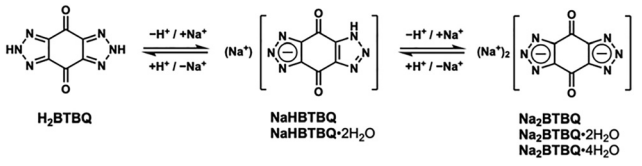

Scheme 1 Chemical structures of **Na_nH_{2-n}BTBQ** (n = 0, 1, 2).

Results and discussion

Hydration and crystal structures

NaHBTBQ was synthesized according to a previously reported method,[35] and then three types of **Na_nH_{2-n}BTBQ** (n = 0, 1, 2) with different H^+/Na^+ ratios were successfully obtained by reaction with acid or base (see the SI for details). Elemental analysis and single-crystal X-ray structural analysis revealed that the chemical compositions were **H_2BTBQ**, **NaHBTBQ**·$2H_2O$, and **Na_2BTBQ**·$4H_2O$, respectively, where the sodium salts were obtained as hydrates containing crystal water. While previous studies have reported the dihydrate form **H_2BTBQ**·$2H_2O$,[35,36] this time we obtained the anhydrous form **H_2BTBQ**. However, the previous studies obtained the dihydrate only through crystallization in aqueous solutions containing significantly excess water molecules. In addition, as will be discussed below, **H_2BTBQ** does not exhibit water sorption capacity up to RH 100% (Fig. 3). Therefore, the dihydrate form is believed to be a kinetically obtained metastable state. In particular, we confirmed that the number of water molecules in the hydrate increased as the number of Na^+ ions increased through H^+/Na^+ exchange in **Na_nH_{2-n}BTBQ**.

Single-crystalline samples were successfully obtained by optimizing the crystallization conditions for **H_2BTBQ**, **NaHBTBQ**·$2H_2O$, and **Na_2BTBQ**·$4H_2O$ (Fig. S2). Single-crystal X-ray structural analysis confirmed the same crystal structures as those reported in previous studies[35,36] (Fig. 1; see also Fig. S3–S5 and Table S1). Although all these structures have already been reported separately in the previous studies, here we shall comprehensively compare and discuss the crystal structures and hydration states of **Na_nH_{2-n}BTBQ** with changing H^+/Na^+ ratio. **H_2BTBQ** was obtained as an anhydrate (Fig. 1a and b). The crystal structure at 100 K possesses a space group of monoclinic $P2_1/c$ with half a crystallographically independent **H_2BTBQ** molecule, containing two **H_2BTBQ** molecules per unit cell (Table S1). The protons on **H_2BTBQ** are located on the N atom at the 2-position of the 1,2,3-triazole ring, forming one-dimensional hydrogen-bonded chains along the $a + b$ and $b - a$ directions *via* N–H···N double hydrogen bonds ($d_{N\cdots N}$ = 2.946 Å) with the 1,2,3-triazole rings of adjacent molecules (Fig. 1a). These hydrogen-bonded chains stack *via* π–π interactions ($d_{\pi\cdots\pi}$ = 3.218, 3.491 Å) along the $b - a$ and $a + b$ directions, respectively, forming aligned layers within the *ab* plane. In the crystal, two types of layers with different orientations stack alternately along the *c*-axis, forming a three-dimensional structure through inter-layer N–H···N hydrogen bonds ($d_{N\cdots N}$ = 2.997 Å) between 1,2,3-triazole rings of adjacent layers (Fig. 1b). Thus, **H_2BTBQ** was obtained as an anhydrate presumably because the rigid, planar **H_2BTBQ** molecules form a dense molecular assembly through strong double hydrogen

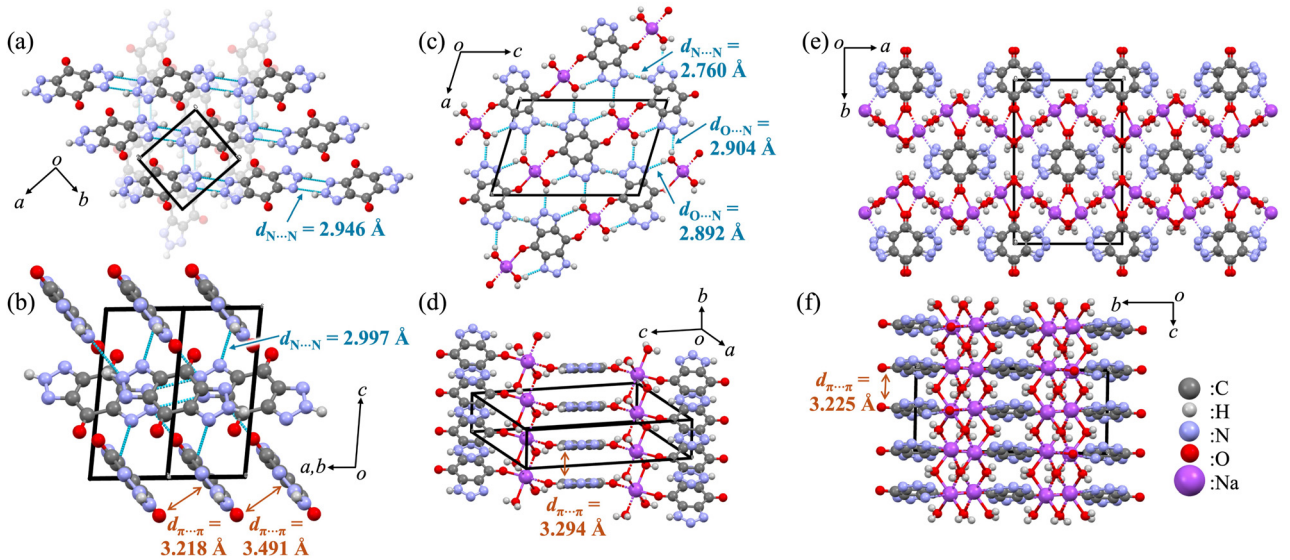

Fig. 1 Crystal structures of (a), (b) **H_2BTBQ**, (c), (d) **NaHBTBQ**·2H_2O, and (e), (f) **Na_2BTBQ**·4H_2O at 100 K. The light-blue dashed lines indicate the hydrogen bonds.

bonds and π–π interactions, preventing the stable inclusion of crystal water.

NaHBTBQ·2H_2O was obtained as a dihydrate (Fig. 1c and d). The crystal structure at 100 K possesses a space group of monoclinic *P*2/*n* with 0.5 **HBTBQ**$^-$ molecules, 0.5 Na^+ ions, and 1 water molecule as crystallographically independent species, containing 2 formula units per unit cell (Table S1). In the crystal, $[Na(H_2O)_2]_\infty$ chains, where Na^+ ions are bridged by two water molecules, and π-stacked columns of **HBTBQ**$^-$ extend along the *b*-axis (Fig. 1c and d). In the $[Na(H_2O)_2]_\infty$ chain, the carbonyl O atom of the **HBTBQ**$^-$ molecule coordinates to Na^+, and four water molecules bridging the Na^+ ions along the *b*-axis also coordinate to Na^+, resulting in a six-coordinate structure (Fig. S3a). Meanwhile, the **HBTBQ**$^-$ columns formed π-stacking with a distance of $d_{\pi\cdots\pi}$ = 3.294 Å (Fig. 1d). The water molecules in the $[Na_2(H_2O)_2]_\infty$ chains form O–H···N hydrogen bonds ($d_{O\cdots N}$ = 2.892, 2.904 Å) with the N atoms at the 2- and 3-positions of the 1,2,3-triazole ring of **HBTBQ**$^-$, thereby forming a two-dimensional hydrogen bond network within the *ac* plane (Fig. 1c). The protons on **HBTBQ**$^-$ are located on the N atom at the 1-position of the 1,2,3-triazole ring, forming inter-columnar N–H···N hydrogen bonds ($d_{N\cdots N}$ = 2.760 Å) with the 1,2,3-triazole rings of adjacent molecules. Note that the protons in the N–H···N hydrogen bonds are disordered in two positions, indicating these are low-barrier hydrogen bonds (LBHBs). Thus, **NaHBTBQ**·2H_2O was obtained as a dihydrate with stable crystal water, likely because the reduction of protons on **BTBQ** *via* H^+/Na^+ exchange prevented the formation of strong double hydrogen bonds as seen in **H_2BTBQ** and facilitated the electrostatic interactions and the flexible coordination geometry of Na^+.

Na_2BTBQ·4H_2O was obtained as a tetrahydrate containing even more crystal water than **NaHBTBQ**·2H_2O (Fig. 1e and f). The crystal structure possesses a space group of monoclinic *C*2/*c* with 0.5 **BTBQ**$^{2-}$ molecules, 1 Na^+ ion, and 2 water molecules (1 + 0.5 + 0.5 molecules) as crystallographically independent species, containing 4 formula units per unit cell (Table S1). In the crystal, two water molecules bridge two Na^+ cations, and these $[Na_2(H_2O)_2]$ units are further connected by two water molecules to form $[Na_2(H_2O)_4]_\infty$ zig-zag layers within the *ac* plane (Fig. 1e and Fig. S4a). Between these layers, π-stacked columns of **BTBQ**$^{2-}$ extend along the *c*-axis. In the $[Na_2(H_2O)_4]_\infty$ layer, Na^+ forms a six-coordinate structure based on coordination with four water molecules bridging the Na^+ ions as well as with the carbonyl O atom and the N atom on the 1,2,3-triazole ring of the **BTBQ**$^{2-}$ molecule (Fig. S4b). The **BTBQ**$^{2-}$ molecules formed π-stacked columns with a distance of $d_{\pi\cdots\pi}$ = 3.225 Å (Fig. 1f). Furthermore, the water molecules in the $[Na_2(H_2O)_4]_\infty$ layer formed O–H···N hydrogen bonds ($d_{O\cdots N}$ = 2.847, 2.921 Å) with the carbonyl O atoms and N atoms on the 1,2,3-triazole ring of **BTBQ**$^{2-}$, or O–H···O and O–H···N electrostatic interactions ($d_{O\cdots O}$ = 3.019 Å, $d_{O\cdots N}$ = 3.260 Å), constructing a three-dimensional crystal structure (Fig. S4c). Thus, **Na_2BTBQ**·4H_2O was obtained as a tetrahydrate incorporating more crystal water due to the complete loss of protons on **BTBQ** *via* H^+/Na^+ exchange, which prevented the formation of strong hydrogen bonds between **BTBQ**s, and the further increase in the number of Na^+ ions compared to **NaHBTBQ**·2H_2O.

As described above, the sequential substitution of H^+ in **H_2BTBQ** with Na^+ demonstrated that the flexibility of the crystal lattice and the capacity to incorporate water molecules into the crystal can be controlled in a stepwise manner.

Thermal properties and water sorption behaviors

To investigate the dehydration behavior of crystal water and the reversibility of hydration, thermal measurements and water vapor sorption isotherm measurements were performed using powder samples. The powder samples used for the measurements were confirmed to have the same chemical compositions

and crystal structures as the single crystals described above by elemental analysis and PXRD measurements (Experimental section and Fig. S5 in the SI).

The thermal stability of each sample was evaluated by TG measurements. Weight losses accompanied by exothermic peaks due to thermal decomposition were observed at approximately 570–580 K for **H_2BTBQ** and 540–600 K for **NaHBTBQ**·$2H_2O$, while the onset of thermal decomposition was observed at a temperature above approximately 700 K for **Na_2BTBQ**·$4H_2O$ (Fig. S6). For the hydrated salts **NaHBTBQ**·$2H_2O$ and **Na_2BTBQ**·$4H_2O$, in addition to the weight loss due to thermal decomposition, weight losses accompanied by endothermic peaks were observed at approximately 300–330 K and 380–430 K (1.3 and 14.3 wt%) for **NaHBTBQ**·$2H_2O$, and at approximately 310–350 K and 360–410 K (11.6 and 11.5 wt%) for **Na_2BTBQ**·$4H_2O$ (Fig. 2a and Fig. S6). Except for the first-step weight loss of **NaHBTBQ**·$2H_2O$, these weight losses correspond to the desorption of two water molecules each (theoretical values: 14.6 wt% for **NaHBTBQ**·$2H_2O$, and 11.8 wt% for **Na_2BTBQ**·$4H_2O$). This result indicates that crystal water desorbs upon heating in **NaHBTBQ**·$2H_2O$ and **Na_2BTBQ**·$4H_2O$, and the salts exist as stable anhydrates at high temperatures. The first-step weight loss of **NaHBTBQ**·$2H_2O$ corresponds to $0.2H_2O$, suggesting moisture adsorbed on the surface/interface of the powder sample, or a small amount of another hydrate state containing more than 2 crystal water molecules as a small peak was observed at $2\theta \sim 15^\circ$ in the PXRD pattern (Fig. S9). In **Na_2BTBQ**·$4H_2O$, as reported in the previous research,[36] four molecules of crystal water per formula unit are desorbed sequentially in two steps of two molecules each.

To investigate the water desorption process in detail, DSC measurements were performed. For the anhydrous **H_2BTBQ**, no peaks indicative of phase transitions were observed in the measurement range of 173–443 K (Fig. S7a). On the other hand, for **NaHBTBQ**·$2H_2O$, endothermic peaks were observed at 335 and 406 K with ΔH = 4.40 and 120.40 kJ mol^{-1}, respectively, only during the initial heating process (Fig. S7b). These correspond to the desorption of surface-adsorbed water and two molecules of crystal water as observed in the TG chart, respectively. These endothermic peaks were not observed in the subsequent thermal cycles; instead, small anomalies were observed at approximately 350 K on heating and 300 K on cooling. Similarly, for **Na_2BTBQ**·$4H_2O$, endothermic peaks corresponding to the two-step water desorption were observed at 348 and 403 K with ΔH = 100.9 and 114.1 kJ mol^{-1}, respectively, only during the initial heating process (Fig. 2b). In the subsequent thermal cycles, these peaks were absent, and a small endothermic peak (ΔH = 0.67 kJ mol^{-1}) at approximately 330 K on heating and a small anomaly at approximately 280 K on cooling were observed. Notably, the enthalpy changes associated with water desorption were estimated to be 60.20 kJ (mol-H_2O)$^{-1}$ for **NaHBTBQ**, and 50.45, 57.05 kJ (mol-H_2O)$^{-1}$ for **Na_2BTBQ**, which exceed the enthalpy of vaporization of bulk water (40.65 kJ mol^{-1} at 373 K).[37] The structural changes were observed in variable-temperature PXRD at the temperatures where the weight losses in TG and the large endothermic peaks

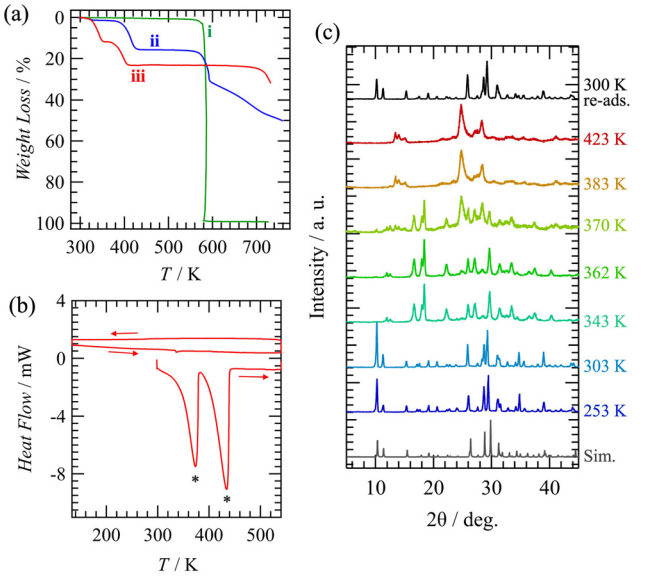

Fig. 2 (a) TG charts of (i) **H_2BTBQ**, (ii) **NaHBTBQ**·$2H_2O$, and (iii) **Na_2BTBQ**·$4H_2O$. (b) DSC chart of **Na_2BTBQ**·$4H_2O$. The asterisks in (b) indicate the endothermic peaks corresponding to the two-step water desorption. (c) Variable-temperature PXRD patterns of **Na_2BTBQ**·$4H_2O$ during water desorption followed by water re-adsorption.

in DSC were observed (Fig. 2c and Fig. S9), which may contribute to the large desorption enthalpies. **NaHBTBQ**·$2H_2O$ and **Na_2BTBQ**·$4H_2O$ can be dehydrated under milder conditions than zeolites; nevertheless, they exhibit water desorption enthalpies surpassing those of reported silica gels[38] and non-porous inorganic salt hydrates,[39] and as large as porous zeolites and MOFs,[40] demonstrating their high potential comparable to non-porous organic calcium salt hydrates[32,33] as promising water adsorption thermal storage materials (Table S2).

To examine the reversibility of crystal water desorption, water vapor sorption isotherms were measured at 298 K. Measurements were performed using anhydrates obtained by dehydration under vacuum heating (see the SI for details). **H_2BTBQ**, originally obtained as an anhydrate, showed only slight adsorption behavior attributed to physisorption on the surface (Fig. S8a). This result strongly supports that the dihydrate form reported in the previous studies is a metastable state that was kinetically obtained in water-excess conditions. In contrast, **NaHBTBQ**, originally obtained as a dihydrate, showed steep water adsorption at P/P_0 = 0.13, followed by a plateau corresponding to $2H_2O$ on the adsorption process (Fig. S8b). On the desorption process, adsorbed crystal water was not desorbed even at the lowest measurement pressure of P/P_0 = 0.04, indicating a large hysteresis of this sorption process. On the other hand, **Na_2BTBQ** showed steep and distinct water adsorption of two molecules each at P/P_0 = 0.05 and 0.96 on the adsorption process (Fig. 3). When reaching P/P_0 = 0.96, P/P_0 shows a transient decrease followed by re-increase. This is because there is a high activation barrier between dihydrate and tetrahydrate due to the involved large structural modulation; at P/P_0 = 0.96, the dihydrate overcomes the high activation

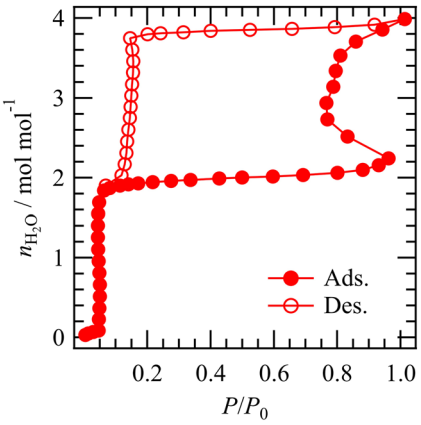

Fig. 3 Water vapor sorption isotherm of **Na_2BTBQ** at 298 K.

barrier to form tetrahydrate, rapidly absorbing water causing the partial pressure to drastically decrease, resulting in a non-equilibrium state. During the desorption process, desorption of two molecules was observed at P/P_0 = 0.15 showing large hysteresis. The second-step water desorption was not observed in the current pressure range, where the lowest measurement pressure on desorption process is P/P_0 = 0.07 exceeding the anhydrate-to-dihydrate plateau pressure on adsorption process (P/P_0 = 0.05). Still, the anhydrate/dihydrate water sorption could show pressure hysteresis involving drastic structural modulation as observed in the dihydrate/tetrahydrate water sorption. These results reveal that **Na_2BTBQ**·4H_2O can reversibly and sequentially adsorb/desorb water accompanied by large pressure hysteresis.

To understand the observed reversible water sorption process in more detail, structural changes during water desorption by heating and subsequent water re-adsorption by exposure to water vapor were investigated by PXRD measurements (Fig. 2c and S9). For both **NaHBTBQ**·2H_2O and **Na_2BTBQ**·4H_2O, the PXRD patterns changed drastically in the temperature range where water desorption was observed in DSC measurements. This suggests that the dehydrated states are in crystalline states different from the original hydrated states. Particularly for **Na_2BTBQ**·4H_2O, the molecular assembly structure was drastically modulated in the temperature ranges above 343 K and 383 K, which correspond to the structures of **Na_2BTBQ**·2H_2O and **Na_2BTBQ**, respectively. Furthermore, upon exposure of the dehydrated **NaHBTBQ** and **Na_2BTBQ** to water vapor, they were reversibly converted back to the original **NaHBTBQ**·2H_2O and **Na_2BTBQ**·4H_2O structures, respectively. Thus, we revealed that both **NaHBTBQ**·2H_2O and **Na_2BTBQ**·4H_2O are capable of reversible water sorption accompanied by significant structural modulation. The observed large hysteresis in water sorption is likely due to the involved significant structural modulation for water sorption into a dense, non-porous molecular assembly.

For the two-step water sorption observed in **Na_2BTBQ**, the relative stability of water molecules in the **Na_2BTBQ**·4H_2O crystal was evaluated using DFT calculations (see the SI for details). In the crystal structure of **Na_2BTBQ**·4H_2O, there are three inequivalent water molecules per formula unit: one molecule each containing O1 and O2, and two molecules containing O3 (Fig. S4). Therefore, the two-step dehydration process is divided into a step where O1 and O2 desorb together (1 molecule each) and a step where two O3 molecules desorb. However, the coordination bond lengths and hydrogen bond lengths (or electrostatic inter-atomic distances) around the water molecules containing O1, O2, and O3 shows no significant differences, suggesting only slight differences in their stability within the crystal (Fig. S10 and Table S3). Therefore, we evaluated the interaction energies of the water molecules with the host crystal using DFT calculations. The results suggested that the O1/O2 water molecules interact more strongly by approximately 1.8 kJ mol^{-1} than two O3 molecules (Table S4). Therefore, the desorption of two O3 molecules likely occurs in the first step, followed by the simultaneous desorption of O1 and O2 in the second step. Such subtle differences in the stability of crystal water lead to the unique two-step reversible water sorption in **Na_2BTBQ**·4H_2O.

Dielectric responses and ionic conductivities

Finally, to investigate the physical property changes induced by the two-step reversible water sorption in **Na_2BTBQ**, dielectric responses and proton conductivities were evaluated for anhydrate, dihydrate, and tetrahydrate using the alternating-current (AC) impedance method. For the measurements of hydrated salts, the compressed pellets were coated with an inert resin to suppress water desorption during heating (see the SI for details).

The real part (ε_1) and imaginary part (ε_2) of the dielectric constant of the anhydrate showed a monotonic increase with heating and slight frequency dependence, with small ε_1 values ranging from 3.9 at 300 K to 10.3 at 500 K at 1 kHz (Fig. 4a and b). Although the crystal structure of anhydrous **Na_2BTBQ** was not obtained, since the crystal consists only of Na^+ and **$BTBQ^{2-}$**, the observed temperature/frequency dependence is attributed to slight Na^+ dynamics. In contrast, the dihydrate and tetrahydrate after water adsorption showed large dielectric responses with significant temperature and frequency dependence, revealing that the dielectric response of **Na_2BTBQ** can be reversibly switched by water sorption (Fig. 4c–f). The ε_1 of the dihydrate increased monotonically from 134.8 at 300 K to 245.7 at 340 K at 1 kHz, exhibiting a dielectric constant approximately 50 times larger than that of the anhydrate (Fig. 4c). Similarly, ε_2 increased monotonically from 106.8 at 300 K to 455.2 at 340 K at 1 kHz, showing typical behavior for ionic conduction (Fig. 4d). The tetrahydrate also showed similar temperature/frequency dependence characteristic for ionic conduction, where both ε_1 and ε_2 increase monotonically with heating accompanied by significant frequency dependence (Fig. 4e and f; ε_1 at 1 kHz: 14.4 at 300 K to 46.9 at 360 K). Interestingly, while **Na_2BTBQ** shows a large dielectric response upon hydration, the dihydrate exhibited a higher dielectric constant, *i.e.* a higher electric field responsiveness, than the tetrahydrate.

In **Na_2BTBQ**·2H_2O and **Na_2BTBQ**·4H_2O, where significant temperature/frequency dependence was observed in the complex dielectric constant, semicircular traces characteristic of ionic conduction were confirmed in the Nyquist plots of complex impedance Z^* (Fig. 5a and Fig. S11a). Ionic

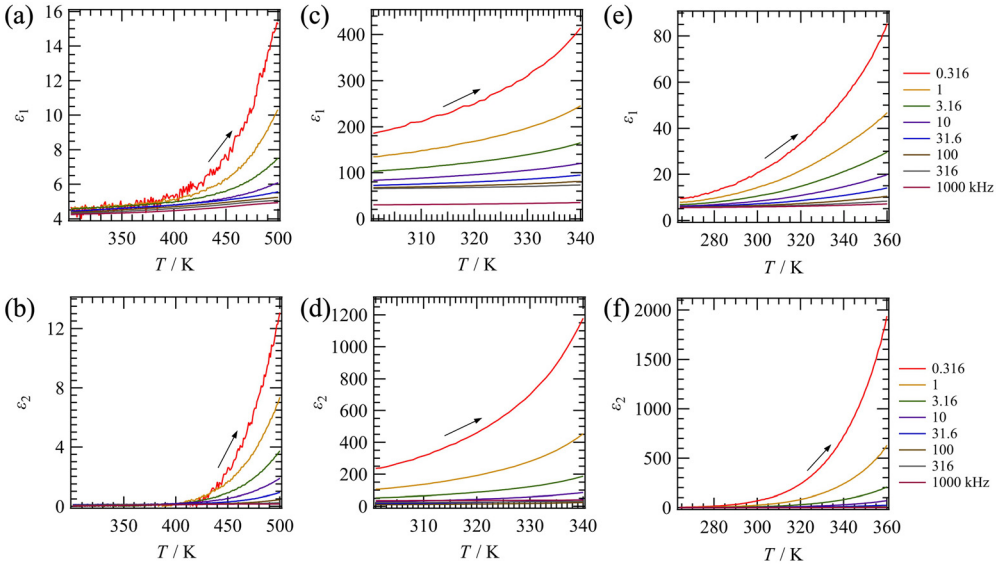

Fig. 4 Temperature(T)- and frequency(f)-dependent (a), (c), (e) real (ε_1) and (b), (d), (f) imaginary (ε_2) parts of the dielectric constants of (a), (b) **Na_2BTBQ**·$0H_2O$, (c), (d) **Na_2BTBQ**·$2H_2O$, and (e), (f) **Na_2BTBQ**·$4H_2O$ on heating processes.

conductivities were estimated by fitting the frequency dependence of Z^*. The estimated conductivities of both **Na_2BTBQ**·$2H_2O$ and **Na_2BTBQ**·$4H_2O$ increased on heating, indicating thermally activated ionic conduction (Fig. 5b). **Na_2BTBQ**·$2H_2O$ exhibited higher conductivity than **Na_2BTBQ**·$4H_2O$ at the same temperature range, consistent with its higher dielectric constant. The maximum conductivity reached 2.0×10^{-7} S cm^{-1} at 340 K for **Na_2BTBQ**·$2H_2O$ and 3.5×10^{-7} S cm^{-1} at 360 K for **Na_2BTBQ**·$4H_2O$, respectively. Temperature dependence of their conductivities showed Arrhenius-type behavior, from which the activation energies were estimated to be 0.450(10) and 0.557(5) eV for **Na_2BTBQ**·$2H_2O$ and **Na_2BTBQ**·$4H_2O$, respectively (Fig. S11b and S12). These results demonstrate the hydration-induced switching of ionic conductivity in **Na_2BTBQ**.

The origin of the ionic conduction observed in **Na_2BTBQ**·$2H_2O$ and **Na_2BTBQ**·$4H_2O$ is considered to be Na^+ or H^+ conduction. In the crystal structure of **Na_2BTBQ**·$4H_2O$, a possible proton conduction pathway based on the Grotthuss mechanism[41] exists along the c-axis (Fig. S13). However, the protons need to migrate over long distances of $d_{O\cdots N}$ = 2.921, 3.260 Å, implying the contribution to ionic conduction is small. Furthermore, since the activation energy estimated from the temperature dependence of ionic conductivity is 0.557(5) eV, which is higher than the typical value 0.1–0.4 eV for the Grotthuss mechanism, the conduction is likely due to H^+ conduction based on the vehicle mechanism[42] or Na^+ conduction. Considering that there is no proton source other than crystal water in the assembly structure, Na^+ ions are the more plausible origin of ionic conduction. Although the crystal structure of **Na_2BTBQ**·$2H_2O$ has not been obtained, Na^+ ion conduction is considered to occur similarly. Even in the anhydrate, temperature/frequency dependence of the dielectric constant was observed (Fig. 4a and b), which imply slight Na^+ ion dynamics. These results suggest that the coordination of water

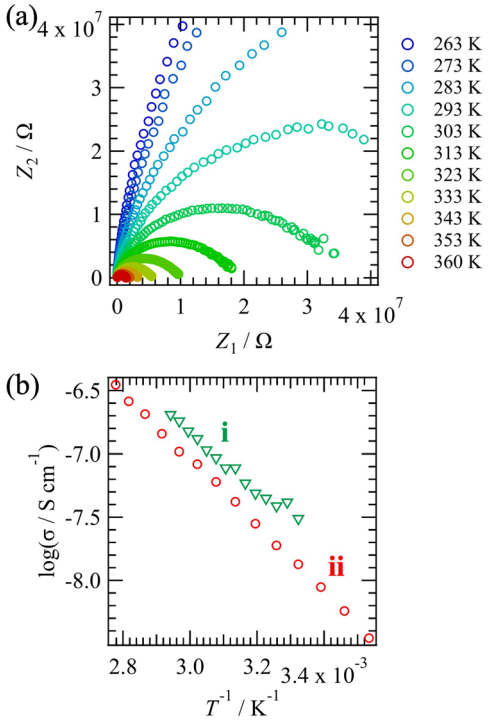

Fig. 5 (a) Nyquist plots for the complex impedance of **Na_2BTBQ**·$4H_2O$ at various temperatures. (b) Temperature dependences of the ionic conductivities for (i) **Na_2BTBQ**·$2H_2O$ and (ii) **Na_2BTBQ**·$4H_2O$.

molecules to Na^+ upon hydration weakens the interaction between Na^+ and **HBTBQ**$^-$ or **BTBQ**$^{2-}$, thereby promoting Na^+ conduction. Indeed, in previous studies on ionic conductors, coordination of solvent molecules to metal ions has been reported to promote ionic conduction by weakening the electrostatic interaction with the crystal lattice.[43] These results

demonstrate that **Na_2BTBQ** exhibits two-step switching of Na^+ ionic conductivity induced by two-step reversible water sorption.

On the other hand, **H_2BTBQ** showed no dielectric response, with ε_1 values of 3.5–3.7 independent of temperature and frequency in the measurement range of 300–400 K (Fig. S14a and b). **NaHBTBQ** showed characteristic ionic conduction behavior with monotonic increase of ε_1 and ε_2 on heating accompanied by frequency dependence for both the anhydrate and dihydrate (Fig. S14c–f). However, both ε_1 and ε_2 values of **NaHBTBQ** were small compared to **Na_2BTBQ**, and ionic conductivity could not be estimated from the frequency dependence of Z^*. Notably, unlike **Na_2BTBQ**, **NaHBTBQ** exhibited a higher dielectric constant in the anhydrate than in the hydrate. Therefore, the origin of ionic conduction observed in **NaHBTBQ** is considered to be protons, and crystal water inhibits proton conduction and/or the anhydrate possesses more efficient conduction pathways.

Conclusions

In conclusion, we have successfully developed a dense organic salt system, **Na_nH_{2-n}BTBQ** (n = 0, 1, 2), that exhibits reversible hydration-induced functional switching. By sequentially substituting the protons of the rigid π-planar molecule **H_2BTBQ** with sodium ions, we were able to modulate the flexibility of the crystal lattice and its affinity for water molecules. Specifically, the disodium salt **Na_2BTBQ** demonstrated a unique reversible two-step water sorption capability involving four water molecules. This process is accompanied by a large endothermic enthalpy change that surpasses the heat of vaporization of water, highlighting its potential for high-performance thermal energy storage and cooling applications. While we have not evaluated the adsorption/desorption kinetics in detail, the TG curves show that the weight loss associated with water desorption completes within 10–20 K (Fig. S6), suggesting that the conversion between different hydration states occurs on the order of minutes. This remarkably rapid kinetics compared with previously reported inorganic salts likely reflects the flexibility of the organic alkali-metal salts. Furthermore, the hydration of **Na_2BTBQ** triggers a significant switching of ionic conductivity, attributed to the enhanced mobility of hydrated sodium ions. During water adsorption/desorption, **Na_2BTBQ**·$4H_2O$ is expected to expand and contract along the a and b axes (Fig. 1e; perpendicular to the π-stacking direction of **$BTBQ^{2-}$**). However, during the AC impedance measurements, no severe cracks were found even with dense compressed pellets of powder samples after water desorption, which suggests sufficient reversibility for practical applications. This study presents a promising design strategy for developing multifunctional materials that simultaneously achieve large latent heat storage and electrical switching through the reversible hydration of dense organic crystals, opening new avenues for environmentally responsive solid-state devices.

Author contributions

Shiori Harada: formal analysis, investigation (synthesis, thermal analysis, SCXRD, PXRD, sorption isotherms, AC impedance), writing – review & editing. Shun Dekura: conceptualization, investigation (DFT calculations), writing – original draft, supervision, project administration, funding acquisition. Genki Saito: investigation (synthesis). Tetsu Sato: writing – review & editing. Tomoyuki Akutagawa: conceptualization, writing – review & editing, supervision, project administration, funding acquisition.

Conflicts of interest

There are no conflicts to declare.

Data availability

All data supporting this study and its findings are available within the article and the supplementary information (SI). Supplementary information: experimental details, single-crystal structures, PXRD patterns, thermal analysis, reversible water sorption behaviors, 2-step water desorption in **Na_2BTBQ**·$4H_2O$, dielectric responses and ionic conductivities. See DOI: https://doi.org/10.1039/d5tc04307g.

Acknowledgements

This work was supported by a Grant-in-Aid for Scientific Research on KAKENHI (Grant Numbers: JP23K13715, JP25K08582), and Japan Science and Technology Agency ACT-X (Grant Number: JPMJAX23DF) and Core Research for Evolutional Science and Technology (CREST; Grant Number: JPMJCR2542). A part of the calculations in this work has been done using the facilities of the Supercomputer Center, the Institute for Solid State Physics, the University of Tokyo. Elemental analysis in this work was supported by the Central Analytical Facility (CAF) in the Institute of Multidisciplinary Research for Advanced Materials (IMRAM), Tohoku University, Japan.

References

1 R. P. Shibaeva and E. B. Yagubskii, *Chem. Rev.*, 2004, **104**, 5347–5378.
2 T. Higashino and T. Mori, *Phys. Chem. Chem. Phys.*, 2022, **24**, 9770–9806.
3 H. Mori, S. Yokomori, S. Dekura and A. Ueda, *Chem. Commun.*, 2022, **58**, 5668–5682.
4 T. Akutagawa, T. Takeda and N. Hoshino, *Chem. Commun.*, 2021, **57**, 8378–8401.
5 R. Kameyama, T. Fujino, S. Dekura, M. Kawamura, T. Ozaki and H. Mori, *Chem. – Eur. J.*, 2021, **27**, 6696–6700.
6 K. Onozuka, T. Fujino, R. Kameyama, S. Dekura, K. Yoshimi, T. Nakamura, T. Miyamoto, T. Yamakawa, H. Okamoto, H. Sato, T. Ozaki and H. Mori, *J. Am. Chem. Soc.*, 2023, **145**, 15152–15161.
7 T. Fujino, R. Kameyama, K. Onozuka, K. Matsuo, S. Dekura, T. Miyamoto, Z. Guo, H. Okamoto, T. Nakamura, K. Yoshimi, S. Kitou, T.-H. Arima, H. Sato, K. Yamamoto,

A. Takahashi, H. Sawa, Y. Nakamura and H. Mori, *Nat. Commun.*, 2024, **15**, 3028.
8 M. Hemmida, H.-A. K. von Nidda, B. Miksch, L. L. Samoilenko, A. Pustogow, S. Widmann, A. Henderson, T. Siegrist, J. A. Schlueter, A. Loidl and M. Dressel, *Phys. Rev. B*, 2018, **98**, 241202.
9 M. Yamashita, S. Sugiura, A. Ueda, S. Dekura, T. Terashima, S. Uji, Y. Sunairi, H. Mori, E. I. Zhilyaeva, S. A. Torunova, R. N. Lyubovskaya, N. Drichko and C. Hotta, *Npj Quantum Mater.*, 2021, **6**, 1–8.
10 S. Horiuchi, Y. Tokunaga, G. Giovannetti, S. Picozzi, H. Itoh, R. Shimano, R. Kumai and Y. Tokura, *Nature*, 2010, **463**, 789–792.
11 M. Naka and S. Ishihara, *J. Phys. Soc. Jpn.*, 2010, **79**, 063707.
12 K. Kobayashi, S. Horiuchi, R. Kumai, F. Kagawa, Y. Murakami and Y. Tokura, *Phys. Rev. Lett.*, 2012, **108**, 237601.
13 T. Takeda and T. Akutagawa, *Chem. Commun.*, 2022, **58**, 11898–11912.
14 M. Schadt, *Annu. Rev. Mater. Sci.*, 1997, **27**, 305–379.
15 E. Charlet and E. Grelet, *Phys. Rev. E: Stat., Nonlinear, Soft Matter Phys.*, 2008, **78**, 041707.
16 M. Ito, T. Fujino, L. Zhang, S. Yokomori, T. Higashino, R. Makiura, K. J. Takeno, T. Ozaki and H. Mori, *J. Am. Chem. Soc.*, 2023, **145**, 2127–2134.
17 M. Ito, T. Fujino, T. Higashino, M. Hishida and H. Mori, *Angew. Chem., Int. Ed.*, 2025, **64**, e202512609.
18 M. Naka, S. Hayami, H. Kusunose, Y. Yanagi, Y. Motome and H. Seo, *Nat. Commun.*, 2019, **10**, 4305.
19 Y. Yoshii, N. Hoshino, T. Takeda and T. Akutagawa, *J. Phys. Chem. C*, 2015, **119**, 20845–20854.
20 G. Yuan, T. Takeda, N. Hoshino and T. Akutagawa, *J. Phys. Chem. C*, 2020, **124**, 1861–1871.
21 Y. Sunairi, S. Dekura, A. Ueda, T. Ida, M. Mizuno and H. Mori, *J. Phys. Soc. Jpn.*, 2020, **89**, 051008.
22 Y. Hori, S. Dekura, Y. Sunairi, T. Ida, M. Mizuno, H. Mori and Y. Shigeta, *J. Phys. Chem. Lett.*, 2021, **12**, 5390–5394.
23 S. Dekura, M. Mizuno and H. Mori, *Angew. Chem., Int. Ed.*, 2022, **61**, e202212872.
24 C. Sato, S. Dekura, H. Sato, K. Sambe, T. Takeda, T. Kurihara, M. Mizuno, T. Taniguchi, J. Wu, T. Nakamura and T. Akutagawa, *J. Am. Chem. Soc.*, 2024, **146**, 22699–22710.
25 S. Dekura, M. Mizuno and H. Mori, *Chem. Sci.*, 2025, **16**, 19601–19607.
26 S. Yokomori, S. Dekura, T. Fujino, M. Kawamura, T. Ozaki and H. Mori, *J. Mater. Chem. C*, 2020, **8**, 14939–14947.
27 M. Li, T. Takeda, S. Dekura and T. Akutagawa, *J. Phys. Chem. C*, 2024, **128**, 14834–14841.
28 R. Ide, A. Kawasaki, T. Takeda, S. Dekura, N. Hoshino, W. Matsuda, S. Seki and T. Akutagawa, *J. Mater. Chem. C*, 2024, **12**, 3185–3195.
29 O. S. Wenger, *Chem. Rev.*, 2013, **113**, 3686–3733.
30 H. Abe, A. Kawasaki, T. Takeda, N. Hoshino, W. Matsuda, S. Seki and T. Akutagawa, *ACS Appl. Mater. Interfaces*, 2020, **12**, 37391–37399.
31 D. C. Wang, Y. H. Li, D. Li, Y. Z. Xia and J. P. Zhang, *Renewable Sustainable Energy Rev.*, 2010, **14**, 344–353.
32 E. Mastronardo, E. La Mazza, D. Palamara, E. Piperopoulos, D. Iannazzo, E. Proverbio and C. Milone, *Energies*, 2022, **15**, 4339.
33 J.-B. De Maere D'aertrycke, J. Morlot, K. Robeyns, Y. Filinchuk and T. Leyssens, *Food Chem.*, 2020, **325**, 126884.
34 H. Abe, A. Kawasaki, T. Takeda, N. Hoshino, W. Matsuda, S. Seki and T. Akutagawa, *J. Am. Chem. Soc.*, 2021, **143**, 1046–1060.
35 M. Sato, T. Takeda, N. Hoshino and T. Akutagawa, *CrystEngComm*, 2017, **19**, 910–917.
36 H. Bunzen, A. Lamp, M. Grzywa, C. Barkschat and D. Volkmer, *Dalton Trans.*, 2017, **46**, 12537–12543.
37 D. A. McQuarrie and J. D. Simon, *Physical Chemistry: A Molecular Approach*, University Science Books, Sausalito, CA, 1997.
38 H. T. Chua, K. C. Ng, A. Chakraborty, N. M. Oo and M. A. Othman, *J. Chem. Eng. Data*, 2002, **47**, 1177–1181.
39 H. U. Rammelberg, T. Schmidt and W. Ruck, *Energy Procedia*, 2012, **30**, 362–369.
40 H. Kim, H. J. Cho, S. Narayanan, S. Yang, H. Furukawa, S. Schiffres, X. Li, Y.-B. Zhang, J. Jiang, O. M. Yaghi and E. N. Wang, *Sci. Rep.*, 2016, **6**, 19097.
41 C. J. T. de Grotthuss, *Ann. Chim.*, 1806, **58**, 54–74.
42 K.-D. Kreuer, A. Rabenau and W. Weppner, *Angew. Chem., Int. Ed. Engl.*, 1982, **21**, 208–209.
43 Y. Yoshida, T. Yamada, Y. Jing, T. Toyao, K.-I. Shimizu and M. Sadakiyo, *J. Am. Chem. Soc.*, 2022, **144**, 8669–8675.